Scientific Visualization, 2022, volume 14, number 5, pages 16 - 44, DOI: 10.26583/sv.14.5.02

SIVDSR-Dhaze: Single Image Dehazing with Very Deep Super Resolution Framework and Its Analysis

Sangita Roy[1,A], S.S. Chaudhuri[2,B]

[A] ECE Department Narula Institute of Technology Kolkata, India
[B] ETCE Department Jadavpur University Kolkata, India

[1] ORCID: 0000-0002-8898-0183, roysangita@gmail.com
[2] ORCID: 0000-0001-9849-5766, shelism@rediffmail.com

Abstract

Adverse climate conditions can affect digital photography and cause issues such as colour shifting, poor visibility, contrast reduction, and fainted appearance due to the scattering of atmospheric Particulate Matter (APM). Estimating an optimum transmission matrix is the key to success for any single image dehazing technique. The use of VDSR 20-weighted Layers ImageNet classifier within l earning based Super Resolution technique x allows improving any image resolution and leads to noise suppression. High Residual Learning gradient clipping ensures fast convergence of the algorithm followed by denoising and artifacts removal as a result of compression. This key introspection has been exercised in improving resolution of the hazy images with an optical image formation model. In addition, we evaluate the benchmark of established images and make results comparisons to the state-of-the-art methods that shows a consistent improvement in accurate scene transmission estimation resulting in clear, natural haze-free radiance. A plausible consistency between execution speed and processing speed has been achieved.

Keywords: VDSR, Dehazing, APM, optical image formation model, SIVDSR, SIVDSR-Dhaze, MOSF, VIA.

1. Introduction

Atmospheric particulate matter (APM) that is inclusively known as aerosols, is the main cause of scattering, absorption, reflection, and refraction of light in the medium. Photographs of a natural scene under high environmental pollution are known to reduce radiance due to attenuated direct scene transmission and cumulative additive scattered surrounding light familiar as airlight or veiling light [6-12, 18, 20, 30]. The Airlight dominates the distant object scene radiance due to attenuation of direct transmission and diminishes to zero. Ultimately, low contrast and a whitish veil cover the image entirely. To address the problem, single image prior based visibility improvement algorithms are used that dominate in the dehazing research domain. These techniques hinge on a physical-based image formation model combining convexly with the direct scene transmission and airlight. The majority of image dehazing methods recover scene radiance by replacing the layer of haze and rely on a physical image formation model [1, 2, 10, 11] for this. In section 3, this mechanism has been described elaborately with the coefficients of the linear combination that represents the scene transmission (visibility) at each image pixel. A pixel in an RGB image represents the four unknown parameters- a) the scene radiance at each R, G, B colour channel and b) the transmission value. Whereas, the input captured image supplies only three constraints, the intensity of each R, G, B channel. To rectify this indeterminacy, most of the renowned methods rely on additional information about the scene- a) multiple images photographed in dissimilar weather conditions [36], b) polarization angles [35], and c) knowledge of the scene geometry [39]. In recent times, methods have been developed to replace an additional input requirements. This has

been earned by penalizing the physical model with such properties as maximal contrast [38], or by complimentary assumptions on hazy atmosphere. In Fattal [20], the indeterminacy in the computation of transmission has been relaxed by eliminating scattering light. A solution has been formulated to resolve the ambiguity locally with no correlation between the transmission and surface shading functions in slow varying regions. He et al. [18] efficiently stated that there is a lowest intensity patch of pixels among the pixels in the dark (low-intensity) colour channel, known as Dark Channel Prior (DCP). Such pixels are found across the entire image. Transmission estimation is known to be inaccurate in images with a bright wide region-like sky. VDSR is a well-known highly accurate SISR architecture inspired by VGG-net used for ImageNet classification with 20 weight layers. Long threaded cascading small filters form a deep network structure, and correlated information in wide image regions is extracted efficiently. This framework is faster than SISR and the learning convergence rate is also high at training due to adjustable gradient clipping [4]. The area is of great interest and authors have been carrying out research in this field with prior works [6-9, 30].

The dehazing problem is predominantly ill-posed. By designing an efficient regularized filter, dehazing problems can be resolved with the refinement of the coarse estimated airlight. **Over-saturation, halo artifacts, and gradient reversal artifacts problems** have been found in most existing dehazing techniques. Explicitly, the proposed technique refines the TM via super resolution [4] based DM estimation. The technique implements residual learning with significantly high learning rates to optimize a very deep network fast. Convergence speed is high with gradient clipping to ensure training stability. The effectiveness of the algorithm is tested in terms of subjective and objective comparison with the state-of-the-art techniques [17- 22, 29] on three benchmark datasets. This comparison study shows sufficient improvements in DM, TM and following high quality outputs.

The major contributions of the proposed method are: We propose a novel single image VIA (SIVIA) to minimize the effect of poor visibility. The procedure is executed in 3 steps. First, low complexity SRVDSR based depth map estimation followed by TM estimation has been proposed. The atmospheric scattering image formation model is employed to get the original scene radiance. Finally, a super-resolution output image is obtained from the inverting image formation optical model. Experimental results are assessed and compared to the state-of-the-art VIAs using peak signal to noise ratio (PSNR), structural similarity index (SSIM), Naturalness Image Quality Evaluator (NIQE), Blind/ Referenceless Image Quality Evaluator (BRISQUE), and CIEDE2000 showing improved performance. DMs are compared and analyzed. The paper is organized as follows: a literature survey presented in section 2, the proposed technique described in section 3, results arranged in section 4, and section 5 containing the discussion.

Spotlight:

- A novel single image VIA (SIVIA) is proposed to minimize the effect of poor visibility by inverting the atmospheric scattering image formation model with super resolution.
- Low complexity SRVDSR based depth map estimation followed by TM estimation, comparison and analysis, which results in noise reduction.
- The lower bound of transmission has been examined in detail.
- Experimental results are assessed and compared to seven state-of-the-art VIAs using the peak signal-to-noise ratio (PSNR), structural similarity index (SSIM), Naturalness Image Quality Evaluator (NIQE), Blind/ Referenceless Image Quality Evaluator (BRISQUE), and CIEDE2000 show improved performance.
- **SIVDSR-Dhaze**, **SIVDSR-Dhaze**RE outputs obtained.

2. Literature Survey

Light waves encounter numerous microscopic particles as they traverse the transmission medium to reach the image sensors. Atmospheric scattering occurs which results in higher luminance. However, the reflected light waves are themselves also attenuated and scattered

along the path to the image sensors. Such, multiplicative loss causes a decrease in image contrast [10]. Visible light is primarily attenuated in the atmosphere by the scattering phenomenon and the process model is controlled with an extinction coefficient k. Fog is solely responsible for this phenomenon and creates a luminous veil on the way of direct transmission hindering visibility [14]. In 1924, Koschmieder [13] developed a simple relationship between the apparent luminance L of an object at a distance d and its intrinsic luminance L_o and L_f as far end object luminance.

$$L = L_0 e^{-kd} + L_f (1 - e^{-kd}) \quad (1)$$

2.1 Atmospheric Physics Model

In 1975, McCartney proposed the optic based image formation model which is frequently used in image processing applications. The detailed description was presented by Narasimhan in 2000 [35, 36] which modelled atmospheric scattering taking into account the resulting attenuation. Many renowned methods have been developed from this model such as the multiple images fusion method, partial differential equation algorithm, Tan method, Fattal method, Markov Random Field with Bayesian algorithm, He method, and so on. The image formation optical model as shown in figure 1, d stands for the distance between objects of interest and the observer, β (λ) represents the atmospheric scattering coefficient, and λ denotes the wavelength of the light [11, 26, 36].

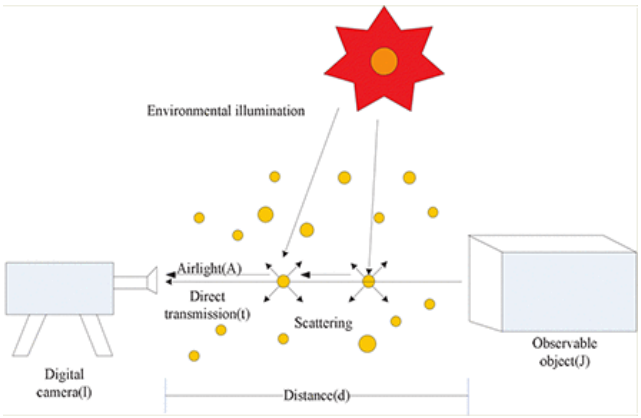

Figure 1. Optical Image Formation Model [28]

2.2 Dehazing Evaluating Techniques

In [2], atmospheric effects are removed from terrain images taken by a forward-looking airborne camera assuming the airlight to be constant over the entire image with known scene depth. Dark Channel Prior (DCP) [18] produces good results with a patch-wise assumption of minimum intensity channel in RGB image. However, some images do not produce satisfactory results due to an underestimated transmittance over dehazing and colour distortion. DCP is a statistical observation for TM estimation accurately. DCP is based on the dark object [1] and the key observation is mostly formed by the local regions (except the sky or hazy regions) that contain pixels with low intensity in at least one of the colour channels. To reduce artifacts, the transmission estimate is further refined based on the alpha matting strategy. **Meng** further explored the merits of the DCP [18]. The technique incorporates a boundary constraint which is a weighted L_1 norm regularization on the transmission estimation produced by DCP. Thus, the overall drawback of DCP alleviates, and sharp edges and bright sky regions are addressed efficiently [19]. **Fattal** proposed a technique depending on the inspection of the distributions of pixels in a small patch of a natural image. These patches stand for one-dimensional structures known as colour lines, in the RGB plane. A low complexity TM is estimated from the computed offset of colour lines to the origin. A refined transmission is formed by a Markov random field model removing the noise and other artifacts due to scat-

tering [20]. **Berman et al.** further investigated the colour consistency observation that examines the colour distribution in a haze-free image. This is well approximated by a discrete set of clusters in the RGB colour space. Furthermore, these pixels in a given cluster are non-local and distributed over the entire image plane. Thus, these pixels are affected asymmetrically by the haze forming cluster leading to haze line. The position of each pixel within the line estimates its transmission level. These haze lines highlight the inconsistency of transmission in different regions of the image. Finally, this is applied to estimate the TM [21]. **Cai et al.** recommend an end-to-end deep CNN model training with synthetic haze to haze-free patch mapping. The technique breaks down into four consecutive steps: features extraction, multi-scale mapping, local extrema, and finally non-linear regression [29]. **Ren et al.** proposed a multi-scale CNN to estimate the TM directly from hazy images trained with synthetic hazy images generated from haze-free images. In turn, the DM is computed followed by application in the light propagation model. The TM is first estimated with a coarse-scale network followed by a fine-scale network [22]. **Ancuti et al. present** a novel straightforward method for local airlight estimation along with the advantage of the multi-scale fusion strategy fusing the multiple versions obtained from distinct definitions of the locality notion. The algorithm is equally effective for the complex night-time dehazing challenge and day-time hazy scene improvement with severe scattering or multiple sources of light [17].

2.3 Super Resolution Techniques

LR images can produce corresponding numerous HR images making SISR image a challenging intractable problem [23]. Earlier mapping of HR images from LR images was insufficient and inefficient. Recent deep learning (DL) based SISR methods are efficient subjectively and objectively. SRCNN was a benchmark for network architecture [24]. SRCNN consists of three-layer CNNs, each with the filter sizes of each layer 64×1×9×9, 32×64×5×5 and 1×32×5×5. These three nonlinear transformations perform patch extraction, nonlinear mapping and reconstruction. The loss function for optimization is mean square error. **5-10 layers of feature learning are common for convolution neural networks (CNN). 50-100 layers of CNNs form very Deep CNN.**

Very Deep Super Resolution (VDSR) improves resolution with a very deep learning technique [4]. With the increase in depth of DL architecture, it becomes difficult to train CNN. Recently, techniques have been developed to converge faster with better results [25]. Huang et al. [31,32] framework was used as a benchmark for comparison of the state-of-the-art results taking into account the same assessment process. Bicubic interpolation is adopted in the YCbCr colour model to take into account the human visual sensitivity to the intensity rather than colour information. Finally, the luminance component is enhanced and denoised with the VDSR network via the final regression layer of the activation network. CIEDE2000 colour distortion is an important parameter for distortion in colour of an image after processing [33, 37].

3. SIVDSR-Dhaze: The Proposed Technique

In this section we describe the proposed single image very deep super resolution SIVDSR [4] based dehazing technique. We consider the technique application from the prospect of the image formation optical model [10]. The VDSR network has been employed for better denoising with super resolution module in the depth estimation stage. Finally, we employ contrast enhancement on the radiance image formed by inverting the image formation optical model.

3.1 Image Formation Optical Model

If N denotes the number of pixels in an RGB colour image I, then 3N possible numbers of equations can be possible. The image formation scattering model in figure 1 is represented as:

$$I_C(x) = J_c(x)t(x) + A_c\big(1 - t(x)\big). \quad (2)$$

Here, $I_C(x)$, $J_c(x)$, and A_c are scalers with the colour components of the channel $c \in \{r, g, b\}$. $J_c(x)$ has 3N unknown radiance. Whereas, there are N unknown transmission t, and 3 unknown atmospheric light A_c. Thus, there are 4N + 3 numbers of unknowns compared to 3N number of equations as in figure 2. This leads to an ill-posed problem that arises due to the ambiguity in the spatially varying t, and hence generating N variables. Thus, at least one extra constraint is required for each pixel to solve the ambiguity [5, 30].

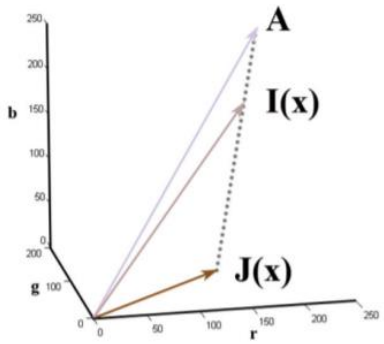

Figure 2. The colour vector I represents a linear combination of J and A in the RGB colour space [18].

Equation 2 can be rewritten as equation 3.

$$I(x) = J(x)t(x) + A(1 - t(x). \quad (3)$$

I(x) represents an observed or received image captured by a camera or sensor. $J(x)$ stands for hazefree image or original scene radiance. $t(x)$ is the transmission map representing the part of the light that arrives the camera without scattering. A stands for the global atmospheric light. $J(x)t(x)$ describes direct decay of light or attenuation due to the scattering of the reflected light in the medium and is expressed as **direct attenuation**. A(1-t(x)) stands for the atmospheric optical shifted component and is named as **airlight**. This is the activity of the atmospheric light with its shift as a result of previously scattering of light, and as a result original scene colour shifts. In equation 3, J(x)t(x) is a multiplicative effect on the scene radiance, whereas A(1-t(x)) is an additive effect. In nutshell, original scene radiance is influenced by multiplicative attenuation phenomena followed by additive airlight shifting which leads to colour fainting as well as shifting. Transmission of the medium represents homogeneous atmosphere as

$$t(x) = e^{-\beta x} \quad (4)$$

According to **Dark Channel Prior (DCP) [18]**, a natural clear RGB image has at least one minimum intensity patch in a channel out of three channels. This minimum intensity patch is almost zero value. This has been observed in over 5000 image datasets.

Now in [18], t(x) is readdressed as

$$J^{Dark}(x) = (J^C(y)) \quad (5)$$

The corresponding received image is as

$$I_{min}(x) = \frac{J^{Dark}(x)}{A^c} \quad (6)$$

$$I_{min}(x) = \frac{(J^C(y))}{A^c} \quad (7)$$

J^C indicates scene radiance in a channel of RGB image. J^{Dark} represents dark channel of J^C. In correspondence to J^{Dark}, observed minimum intensity channel is I_{min}. Again, considering aerial perspective, t(x) can be rewritten as

$$t(x) = 1 - \omega I_{min}(x). \quad (8)$$

ω, the haziness factor adds a realistic appearance to the dehazed image. Thus, finally inverting the image formation optical model of equation 3, the output dehazed image is as

$$J(x) = \frac{I(x) - A}{(t(x), t_0)} + A. \quad (9)$$

where t_0 is the lower bound of the transmission map $t(x)$ and is set as 0.1[18]. From equation 9, when transmission t(x) reaches zero, J(x) becomes an ill-posed equation. To overcome the issue, t_0 is introduced. In [18], A is estimated as 0.1% in the dark channel. In the proposed scheme, atmospheric light consists of 0.1% brightest pixels of each channel which is more realistic and appropriate. Moreover, atmospheric light and DM are estimated in parallel, reducing computational time.

3.1.1 Depth Map [DM] Conceptualization

As discussed above, the DCP technique generates good quality dehazed images at the expense of computational cost. To overcome this, fast depth map estimation is found in the literature [6-9, 30]. The incorporated in dehazing the image formation optical model [10] is a fundamentally ill-posed inverse problem. Thus, DM estimation cannot be obtained in any one way or technique, rather infinite possibilities are there. Whithin this proposed dehazing approach, super resolution technique VDSR [4, Matlab2018a] has been implemented. DM is estimated in a minimum intensity channel denoised by VDSR.

DM estimates the amount of low intensity in the RGB image. The main objective in DM is to find the amount of scene radiance removing noise that corrupts the image during capturing or due to attenuation [6-9, 16-22]. The DM also provides the depth of distance in an image. In the primary stage, DM is considered the minimum intensity channel out of three RGB channels. Still, it has some noise. To refine DM, super resolution based residual image technique [4] has been incorporated.

3.1.2 Transmission map [TM] Conceptualization

TM indicates the amount of light that reaches the camera without attenuation considering the atmosphere to be homogeneous. This transmission is achieved by inverting or complimenting the DMs. Thus, it is better to consider the residue from a unitary image of the same size as the original image [18]. It is defined in equation 8.

3.1.2.1 Importance of Lower Bound of Transmission Map (t_0)

Transmission is kept under control by a lower bound (t_0) as haze prevails in dense haze regions. Transmission may fall at a value of zero making equation 8 an ill-posed inverse problem. To restrict this situation, the lower limit of TM is mandatory. In [18], the lower limit is considered 0.1 as discussed in section 3.1. The variable lower limit of TM has not yet been considered.

3.1.3 Aerial perspective

As mentioned in section 3.1, equations 8 and 9, the atmosphere on a clear day contains a certain amount of particles. These particles create haze at distant objects. Furthermore, the aerial perspective of human vision is the fundamental cue to estimate depth. Due to this effect, distant objects look faint [18]. ω is the parameter known as the haziness factor and most of the SIVMs incorporate it as a constant. But in [7-9], this is the ratio of minimum intensity to maximum intensity in a depth map. Thus, ω is an adaptable parameter depending on the captured atmosphere [6-9] as shown in equation 8.

3.1.3.1 Adaptable Haziness Factor

In [7-9, 30], the adaptive haziness factor was introduced to address the ever changing and inhomogeneous atmosphere producing effective results. It was already established that one of the channels of RGB image is darker than the other two channels, and one patch of that channel is darkest. With this assumption, the adaptable haziness factor is conceptualized

as the ratio of minimum intensity pixel to maximum intensity pixel in the dark channel or DM channel. This assumption has also been incorporated into these proposed techniques.

3.2 Architecture of the Proposed Model

We have proposed a dehazing model in this paper which is novel from the viewpoint/aspect of obtaining the improved restoration of weather corrupted images. This model can be divided into three parts: the atmospheric scattering model, followed by DM estimation in the VDSR network, and enhancement with residual images.

3.2.1 Low complexity Atmospheric Scattering model [6-9, 30]

A DM of low visibility images has been refined through a minimum order statistics filter of linear complexity O(n) followed by improved transmission estimation. An adaptable haziness factor has been proposed by a ratio of minimum intensity to the maximum intensity of the 3-D RGB image vector [7-9]. The extinction coefficient of atmosphere and visible distance (the distance that can be viewed in the image) before and after processing have been presented for each image automatically. Moreover, a simple contrast metric has been applied as the difference between maximum intensity to minimum intensity of 3D RGB image vectors. By inverting the image formation optical model, a clean image is produced by application of the model in section one. The model is applicable for diverse types of low visibility images. The MOSF used for TM recovery is unique in this research work and has been efficiently applied in the algorithms as the transmission estimator which is the main motivation for the fast and good performance of the proposed methods. Dark channel prior is a patch-based technique that gives patch information, whereas MOSF gives artifact-free detailed pixel information at the expense of minimum cost. Depth map and atmospheric light estimation are very important in colour image dehazing. Selecting the correct atmospheric light value is a challenging problem. In our work, the new value is obtained by first estimating the top 0.1% of the brightest pixel in the minimum channel, which mostly is the haze opaque part of the image and the brightest portion of the image followed by the value of the bright channel. Then, the average of the two channels is collected. This method overcomes the deficiency of the dark channel prior and reduces the influence of white objects or sky areas on the whole image. Moreover, scene radiance dehazed image is improved with the VDSR network as shown in figure 3 as the block diagram of the proposed technique. A revised model of figure 3 is shown in figure 4. In figure 4, the depth map is refined with VDSR [4] which develops good quality TM following high quality radiance image.

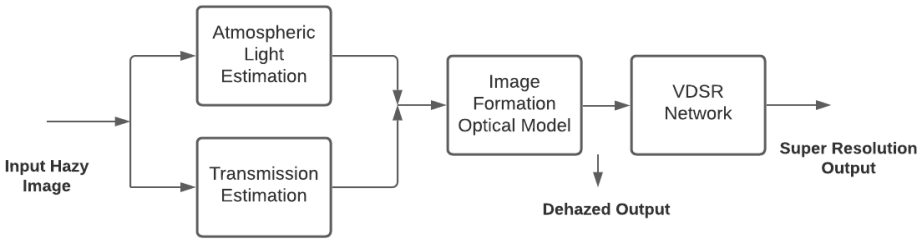

Figure 3. Block Diagram [40]

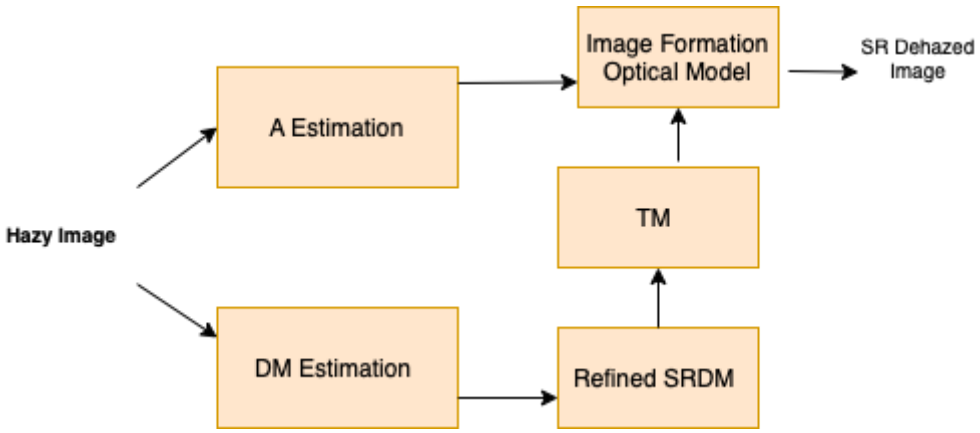

Figure 4. Block diagram of the proposed SRVDSR-Dehaze model, A represents atmospheric light, DM as a depth map, TM as a transmission map

Table I: SIVDSR Algorithms [40].

Algorithm: I (SIVDSR)	
1:	Input hazy image
2:	Atmospheric light estimation,
3:	Depth map estimation
3:	Transmission map estimation
4:	Scene radiance recovery by Image formation Optical model
5:	Output Dehazed Image with VDSR

Table II: SIVDSR-Dehaze: The Proposed Model I.

Algorithm-II (Modification of algorithm I)		
1:	Input hazy image	
2:	Atmospheric light estimation,	Refined Depth map estimation through super resolution technique (three stages: raw depth map (minimum of three channels), 2D bicubic super resolution image, 2D residual image) VDSR network [4]
3:	Refined Transmission map estimation	VDSR RGB Image
4:	Refined Scene radiance through Image formation Optical model	

In algorithm-II, step-II consists of two parallel module-atmospheric light estimation and depth map estimation. Due to parallel operation, step II saves time. This is an added advantage. Algorithm III is by product of algorithm II where the output of algorithm II is enhanced with VDSR RGB, refined RGB image reference with the hazy image as in equation 13.

Table III: SIVDSR-DehazeRE Dehazing: The Proposed Model II.

Algorithm-III (Modification of Algorithm II)		
1:	Input hazy image	
2:	Atmospheric light estimation,	Refined Depth map estimation through super resolution technique (three stages: raw depth map (minimum of three channels), 2D bicubic super resolution image, 2D residual image) VDSR network [4]
3:	Refined Transmission map estimation	VDSR RGB Image
4:	Refined Scene radiance Image formation Optical model	
5:	Output super resolution residual enhanced Dehazed Image	

3.2.2 VDSR Architecture [4]

VDSR [4] is the first pioneering work with Single Image Super Resolution (SISR). As shown in figure. 6, VDSR is a 20-layer VGG-net with a 3x3 kernel. Initially, the learning rate is high for fast convergence. Gradient clipping is used to reduce gradient explosion artifacts. Apart from novel architecture, VDSR has established two more attributes, i) a single model for multiple scales as the SISR operates with different scale factors having a strong relationship with each other. This concept inspires many classical SISR methods. As compared with Super-Resolution Convolutional Neural Network (SRCNN), bicubic interpolation on Low Resolution (LR) image acts as input to the VDSR network. In the training phase, LR bicubic input images of different scale factors are processed in VDSR. The mapping with a smaller scale factor (×2) may also be instrumental for a higher scale factor (x3 or x4), ii) the residual learning is the other unique attribute. Mapping from the bicubic version to High Resolution (HR) is not direct, rather VDSR employs deep CNN for learning the mapping from the bicubic to the residual between the bicubic and HR. The residual learning improves performance and accelerates convergence (see figure 7).

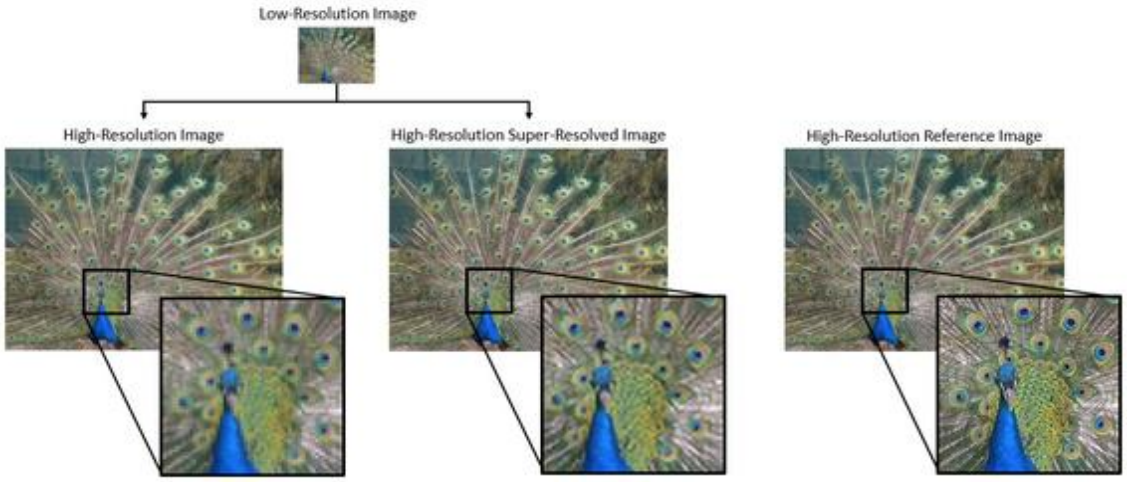

Figure 5. Schematic of the Super-Resolution [4, Matlab18a]

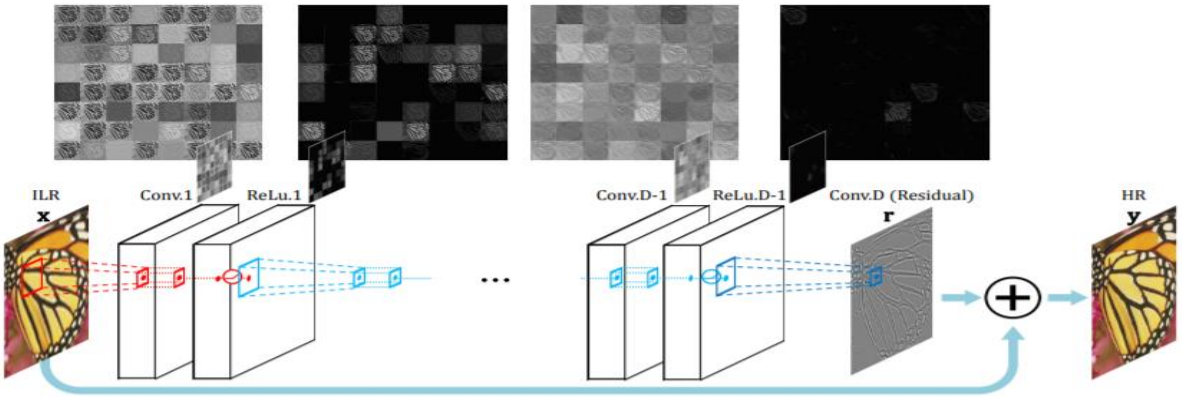

Figure 6. VDSR Network [4]

Hyperparameters used and their attributes:

The parameters used to train our final model are as follows. A network of depth 20 with batch size 64 is considered for training. The momentum and the weight decay parameters are set at 0.9 and 0.0001, respectively. Weights are initialized as [12] with rectified linear units (ReLU), which is a robust and effective module in the network. The network is trained with all images amidst 80 epochs (9960 iterations of 64 batch size). The learning rate is initially set at 0.1 following a decrease by a factor of 10 in every 20 epochs. In short, the learning rate

decreased 3 times with learning stopped after 80 epochs and training time almost 4 hours on GPU Titan Z.

Residual Learning Architecture:

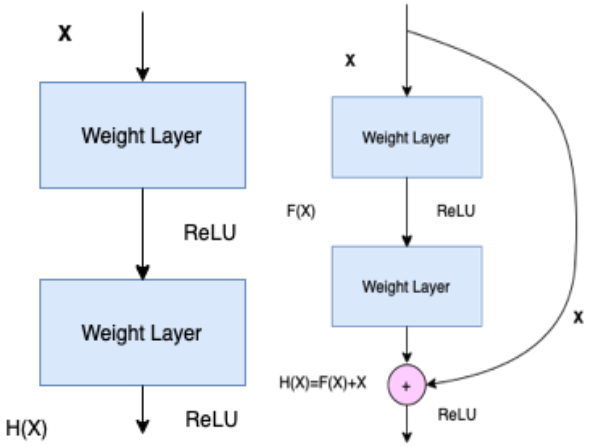

Figure 7. L-R: Traditional CNN framework, Residual Framework

The traditional CNN framework and Residual framework are shown in figure 7. There is a shortcut in the residual framework between every two consecutive layers. This is called a **skip connector**. One such block is called the **Residual network** as in figure 7. Dimension mismatch frequently occurs due to convolution operations in those two consecutive layers. This problem is alleviated by identity mapping for X and F(X). After resizing F(X), H(X) is generated with F(X) and X of the same size. F(X) is the predicted residual,

$$H(X) = F(X) + X \tag{10}$$

Thus, F(X) and X are of the same size. Finally, residual Image is predicted as

$$F(X) = H(X) - X \tag{11}$$

As r is considered as an actual residual image, so that

$$loss\ function = \frac{1}{2}\|r - F(X)\|^2 \tag{12}$$

The loss function is as low as possible. Loss layers collect three inputs; residual estimate, network input (ILR image) and ground truth HR image. The loss is determined as the Euclidean distance between the reconstructed image (the sum of network input and output) and the ground truth.

3.2.3 Residual Enhancement (RE)

This is the last module of SIVDSR techniques as in figure 4, and Table III. The difference between the SR image and the hazy image is added to the dehazed output for enhancement. In **Residual Enhancement step V,** the difference between the VDSR image from step III and the hazy image is amplified and added with the refined scene radiance from step IV. The result is shown in figure 8 below with scene 41, the O-Haze dataset. A comparative visual representation is shown in figure 9, with the left to right images as Hazy, VDSR, Residual, Dehaze, and Residual Enhancement.

$$Residual\ Enhanced\ Image = (Hazy\ Image - VDSR\ Image) * 4 + Radience\ Image \tag{13}$$

Figure 8. Residual Enhancement

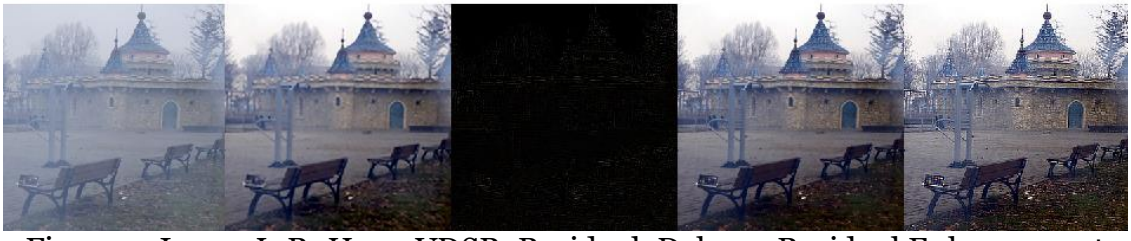

Figure 9. Image L-R: Hazy, VDSR, Residual, Dehaze, Residual Enhancement

3.3 Effect of lower bound

The effect of the lower bound of transmission t_0 (0.9, 0.5, 0.1) on the dehazed image is shown in figures 9, 10, and 11. In [18], the lower bound of transmission has been fixed at 0.1. In this proposed work, different values of transmission lower bound have been incorporated as in eq. (9) and investigated its effect in figures 10, 11, and 12; and tabulated in the corresponding tables IV, V, and VI. Two types of dehazed images have been examined, super-resolution dehazed image and enhanced super-resolution dehazed image. In all three cases of lower bounds, significant results have been found and listed in Tables IV, V, and VI. Parameters (PSNR, SSIM, NIQE, BRISQUE) are used for evaluation and effective results are found at 0.5, and 0.9 respectively.

Figure 10. t_o=0.9, L-R: Hazy Image, Super Resolution Image, Super Resolution enhanced Image

Table IV: Performance with figure 10

t_o =0.9, ω=0.6		**Hazy Image**	**SR radiance image**	**Enhanced SR radiance image**
Full reference parameter [14, 13]	**PSNR**	-	53.0888	52.6401
	SSIM	-	0.9798	0.979
No reference parameter [16, 15]	**NIQE**	1.9013	2.5082	3.0171
	BRISQUE	25.1514	17.449	34.8778

Figure 11. t_o=0.5 L-R: Hazy Image, Super Resolution Image, Super Resolution enhanced Image

Table V: Performance of figure 11.

t0 =0.5, ω=0.6		**Hazy Image**	**SR radiance image**	**Enhanced SR radiance image**
Full reference parameter [14, 13]	**PSNR**	-	52.1919	52.0621
	SSIM	-	0.9717	0.9738
No reference parameter [16, 15]	**NIQE**	1.9013	2.9567	5.927
	BRISQUE	25.1514	19.2671	36.3221

Figure 12. t_0 =.1 L-R: Hazy Image, Super Resolution Image, Super Resolution enhanced Image

Table VI: Performance of figure 12.

t0 =0.1, ω=0.6		**Hazy Image**	**SR radiance image**	**Enhanced SR radiance image**
Full reference parameter [14, 13]	**PSNR**	-	52.1732	52.0057
	SSIM	-	0.9716	0.9735
No reference parameter [16, 15]	**NIQE**	1.9013	2.9615	6.1707
	BRISQUE	25.1514	19.1983	35.5928

3.4 Investigation of DM, TM with histogram and scatter plot

In this section, the proposed SIVDSR-Dehaze net has been described in detail with a histogram and scatter plot. As shown in figures 13, 14, and 15, SIVDSR-Dehaze net performance has been evaluated considering the canon.jpg image [18] as a reference. Two techniques are used. The second technique is the enhancement version of the first one as described in sections 3.2.1 algorithm II, and III. In figure 13, histograms show a clear effect of haze and haze free images of the same scene. The histogram of hazy images reflects dense pixel orientation towards the centre of the graph; whereas histograms of the haze free images are well distributed and Gaussian in nature representing good contrast. Figure 14 illustrates the scatter plots of a) hazy image, b) SR image, c) EnhancedSR image, and d) GT. These scatter plots enumerate the richness in colour and contrast of the proposed techniques in comparison with the hazy ones. The hazy - dehazy image colour cloud plots and histogram are interesting and important in understanding the effectiveness of dehazing schemes. It has been illustrated in figures 13 and 14 by the histogram and colour cloud plotting of the 13_outdoor_hazy.jpg image under the O-Haze data set [17]. It is clearly evident that in hazy images pixel intensities are clustered densely around the upper central part of the intensity scale [0-255]; whereas, in the case of hazefree images, pixel intensities are loosely distributed in almost the entire intensity scale. DM, TM, and radiance images of the same canon.jpg image have been shown in figure 15. It is evident that DMs are darker in the case of haze free images. Consequently, haze free TMs reflect more visibility.

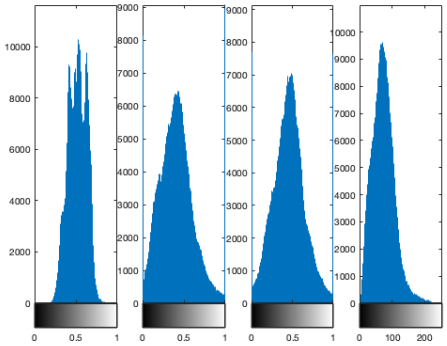

Figure 13. Histogram, L-R: Hazy image, Super resolution image, Enhanced Super resolution image, and GT.

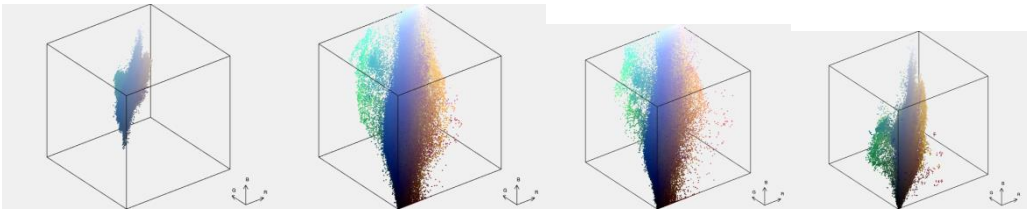

Figure 14. Colour cloud plot of L-R: Hazy image, super resolution image, Enhanced SR image, and GT.

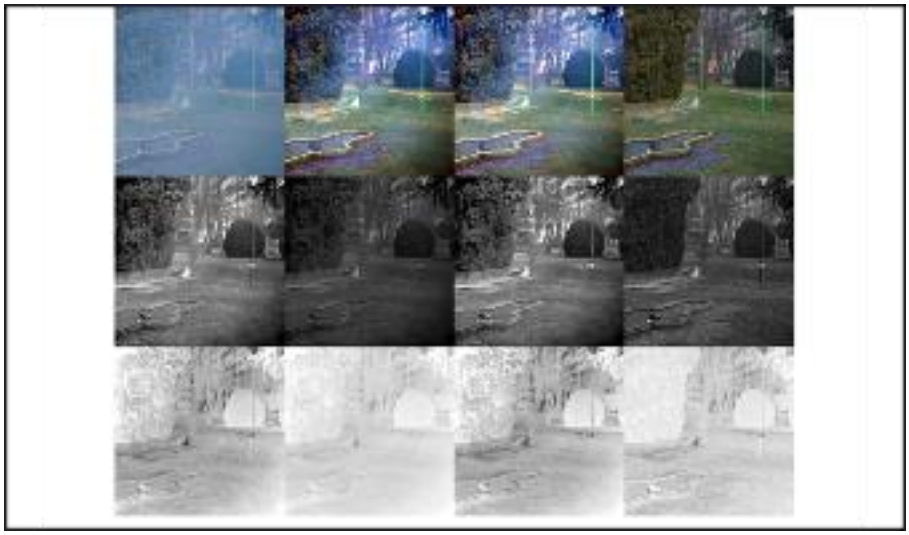

Figure 15. Row-1, L-R: Image: Haze, Super Resolution, Enhanced Super Resolution, GT
Row-2, L-R: Depth Map: Haze, Super Resolution, Enhanced Super Resolution, GT
Row-3, L-R: Transmission Map: Haze, Super Resolution, Enhanced Super Resolution, GT

3.4.1 Difference between DM vs. Residual Map (RM)

Hazy DM, residual DM, SIVDSR-Dehaze DM are shown in figure 16. Corresponding TMs and radiance images are shown in figures 17, and 18 respectively. In figure 18, effective parametric evaluation results are also shown.

Figure 16. Depth map, L-R: Residual Depth Map, Raw depth map, Super resolution Depth Map

3.4.2 Difference between TM vs. Residual TM (RTM)

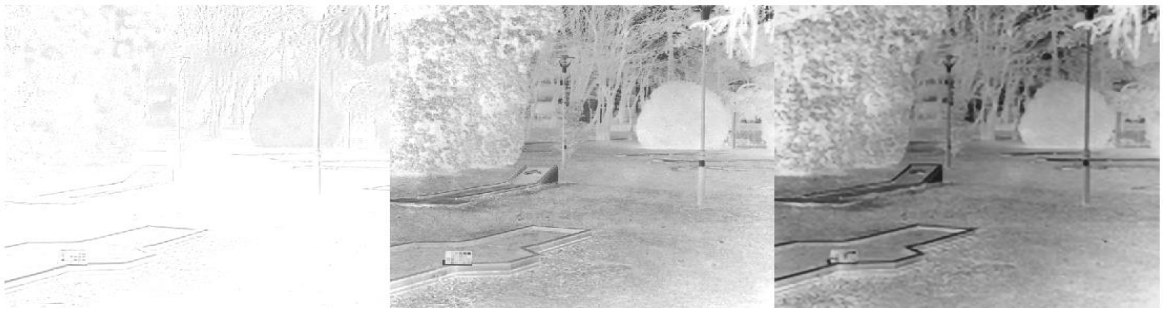

Figure 17. Transmission map of figure 16,
L-R: Residual TM, Raw TM, Super resolution TM

Figure 18. Scene Radiance of scene 13[17], Dehazed output, L-R: Residual Dehazed output, Raw Dehazed output, Super resolution Dehazed output, self-adjusting haziness factor= 0.6423 [7-9], PSNR= 53.5857, 52.1978, 51.4765, SSIM= 0.9819, 0.9715, 0.9635.

3.5 Effect of Adaptable Haziness Factor

In sections 3.1.3 and 3.1.3.1, aerial perspective and adaptable haziness factor were discussed. Here, their effects are investigated. In figures 19 and 20, fixed haziness factors of 0.9 and 0.65 are implemented with hazy, SIVDSR, Residual, SIVDSR-Dhaze, and SIVDSR-DhazeRE images. Furthermore, parametric evaluation (PSNR, SSIM) shows improved results along with qualitative appearances.

The appearance of the hazy image with respect to ground truth, super resolution dehaze, and enhanced super resolution dehaze images are shown in figure 19 along with the depth map and transmission map. The proposed results are visibly improved with increased contrast and higher resolution than GT. Moreover, halo, oversaturated, and gradient reversal artifacts are removed.

Figure 19. Fixed haziness factor (0.9), L-R: hazy, SIVDSR, Residual, SIVDSR-Dehaze, SIVDSR-DhazeRE, GT
Row-1: 43_outdoor_hazy.jpg: PSNR, 15.7524, 13.5508; SSIM, 0.9979, 0.9966 (SIVDSR-Dehaze, SIVDSR-DhazeRE respectively);
Row-245_outdoor_hazyPSNR, 12.8084, 12.1036; SSIM, 0.9799, 0.9843 (SIVDSR-Dehaze, SIVDSR-DhazeRE respectively).

Figure 20. Adaptable haziness factor 0.65, L-R: hazy, SIVDSR, Residual, SIVDSR-Dehaze, SIVDSR-DhazeRE, GT
Row-1: 43_outdoor_hazy.jpg, PSNR,16.9375, 14.2856; SSIM, 9987, 9965 (SIVDSR-Dehaze, SIVDSR-DhazeRE respectively);
Row-2: 45_outdoor_hazyPSNR, 13.8708, 12.9066; SSIM, 0.9814, 0.9862 (SIVDSR-Dehaze, SIVDSR-DhazeRE respectively);

3.6 More Theoretical Analysis with lower bound of transmission

In this section, canon.jpg [18] with dense haze has been tested with our methods using different lower bound of transmission. In figure 21, at t_o 0.1 SIVDSR-DhazeER produces oversaturated, halo, and gradient reversal artifacts. With the increase of t_o, these artifacts are not prominent as in figures 22, and 23.

Figure 21. at t_o =0 .1, L-R: Hazy Image, Oversaturated, gradient reversal, halo effect outputs with the proposed methods (SIVDSR-Dehaze, SIVDSR-DehazeRE)

Figure 22. t_o = 0.5, L-R: Hazy Image, Oversaturated, gradient reversal, halo artifacts outputs with the proposed methods

Figure 23. t_o = 0.9, L-R: Hazy Image, Oversaturated, gradient reversal, halo effect free outputs with the proposed methods

The lower bound of transmission has been experimented with in figures 21, 22, and 23 as 0.1, 0.5, and 0.9 respectively with SIVDSR-Dehazed and SIVDSR-DehazeRE outputs. The image is canon.jpg of size 500x500 [18]. Figures 21, and 22 are showing oversaturated, gradient reversal and halo artifacts resulting at t_o 0.1, and 0.5 respectively. In figure 20 with t_o as 0.9, clear outputs are shown. Thus, this can be established that the lower bound of transmission plays an important role in producing clear outputs. Finally, the fixed value of t_o may not produce the desired output. This leads to variable or adaptable lower bounds of the transmission map estimation. In figures 24, 25, and 26, a detailed study of DM, TM at t_o 0.1. 0.5, 0.9 have been observed.

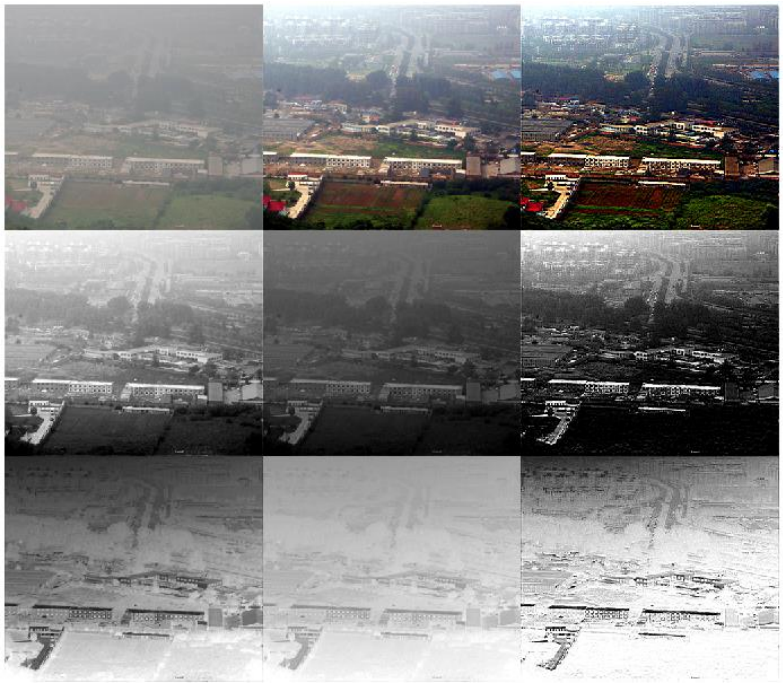

Figure 24. Hazy Image, Oversaturated, gradient reversal, halo effect outputs with the proposed method at t0=0.1,
Row-1: Haze, SIVDSR-Dehaze, SIVDSR-DehazeRE; Row-2:DM of row-1; Row-3:TM of row-1.

Figure 25. Hazy Image, Oversaturated, gradient reversal, halo effect outputs with the proposed method at t0=0.5
Row-1: Haze, SIVDSR-Dehaze, SIVDSR-DehazeRE; Row-2:DM of row-1; Row-3:TM of row-1.

Figure 26. Hazy Image, Oversaturated, gradient reversal, halo effect free outputs with the proposed method at t0=0.9
Row-1: Haze, SIVDSR-Dehaze, SIVDSR-DehazeRE; Row-2:DM of row-1; Row-3:TM of row-1.

4. Experiment

The proposed method is implemented on MATLAB R2018a on a PC with a 2.8 GHz Intel Core 2 Duo Processor. Our proposed model experimented with the O-Haze dataset [17], and [18] to conduct a comprehensive evaluation of the state-of-the-art single image dehazing techniques presented.

Benchmark Used

Benchmark Dataset is used [17-22].

4.1 Dehazing Evaluating Metric

The details of the generator structures and parameter settings are shown in Table VII.

Table VII. Parameter for performance evaluation

Sl. No.	Parameter	Requirement	Type
1	Peak Signal to Noise Ratio (PSNR) [14]	High value	Full Reference
2	Structure Similarity Index Metric (SSIM) [13]	[0-1] in normalized scale high value	Full Reference
3	blind/reference less image spatial quality evaluator (BRISQUE) [15]	Smaller value better performance	No reference
4	Naturalness Image Quality Evaluator (NIQE) [16]	Smaller value better performance	No reference
5	CIEDE2000[33, 37]	Lower value for low colour distortion	No reference

Table VIII. Quantitative Evaluation of figure 27 (PSNR, SSIM) with image size 350x350x3

Parameter	**Dehazed Image**	**Improved Depth Map**	**Improved TM**
PSNR	12.0783	12.4972	20.244
SSIM	0.4374	0.4949	0.6474

Table IX. Quantitative Evaluation of figure 27 (BRISQUE, NIQE)

Parameter	**Hazy Image**	**Depth Map**	**TM**	**Improved Depth Map**	**Improved TM**	**Dehazed Image**
BRISQUE	18.8784	30.5624	12.9649	43.4582	43.4582	18.8747
NIQUE	24.4850	18.8814	18.8793	18.8772	18.8768	43.4582

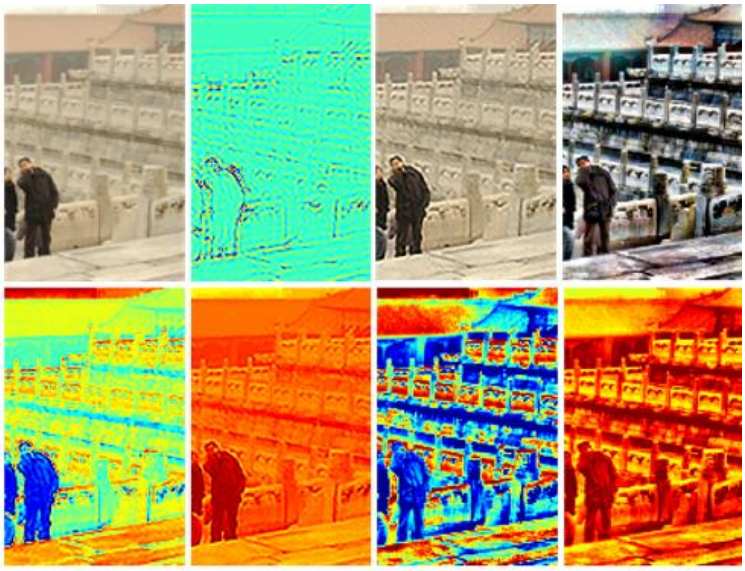

Figure 27. Qualitative Evaluation of gugon.jpg [18],
L-R: Top row- (a) degraded image, (b) residual image, (c) VDSR image, (d) clean image
Bottom row- (e) Hazy DM, (f) TM, (g) recovered DM, (h) recovered TM.

Figure 27 illustrates one scene (gugoon.jpg) [18] as input with our model and each step output has been extracted and compared qualitatively and quantitatively w.r.t hazy counter-part as shown in tables IX, and X.

4.2 Qualitative and Quantitative Evaluation

In figure 28, one hazy image-GT pair [17] is tested with the state-of-the-art methods [17-22, 29], and our methods. Its parametric evaluation is shown in Table X. Figure 29 is the crop/ zoom version of figure 28 for a detailed study.

In order to show the efficiency of the proposed method, we compare results with related traditional methods. This approach performs appreciably with a very dense haze. However, results are often over-saturated because the method does not utilize a physical model to re-cover the image. The results of our method show clearer images with less colour saturation. The peak signal-to-noise ratio (PSNR) is most commonly used to measure the quality of re-construction of hazy images. PSNR is most easily defined via the mean squared error. In our experiment, we use PSNR, SSIM, NIQE, BRISQUE, and Entropy work in [4]. Table XI shows comparable satisfactory results with the proposed methods.

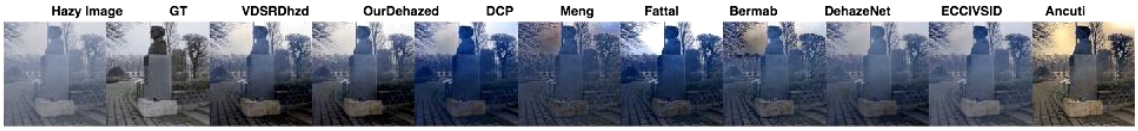

Figure 28. Subjective evaluation with O-Haze dataset [17]. (a) Hazy image, (b) Ground Truth, (c) SIVDSR-Dehaze, (d) SIVDSR-DehazeRE, (e) DCP [18], (f) Meng [19], (g) Fattal [20], h) Berman [21], (i) DehazeNet [29], (j) Ren [22], (k) Ancuti [17]

Table X. Evaluation of Algorithm Performance w.r.t figure 28 (PSNR, SSIM, NIQE, BRISQUE, Entropy) along with ranks

	PSNR	**SSIM**	**NIQE**	**BRISQUE**	**Entropy**
GT	16.7986(2)	0.6818(5)	4.1515(9)	20.1243(10)	7.5171(6)
SIVDSR_Dehaze	16.581(3)	0.6482(6)	4.71(10)	4.4171(3)	7.0958(2)
Dehazed	13.3872(6)	0.6475(7)	3.6772(5)	10.4409(5)	7.7466(10)
DCP	11.6003(10)	0.5949(9)	3.5251(2)	2.5369(1)	7.6295(9)
Meng	11.9278(8)	0.7142(4)	3.532(3)	19.2958(9)	7.0896(1)
Fattal	11.9241(9)	0.6217(8)	3.8544(8)	11.4575(7)	7.211(3)
Berman	13.0319(7)	0.7232(3)	3.6336(4)	13.6197(8)	7.333(5)
DehazeNet	14.9516(4)	0.8383(2)	3.6809(6)	10.5405(6)	7.5696(8)
Ren	17.161(1)	0.9019(1)	3.4389(1)	3.6508(2)	7.2983(4)
Ancuti	13.8383(5)	0.3273(10)	3.7013(7)	8.2222(4)	7.5529(7)

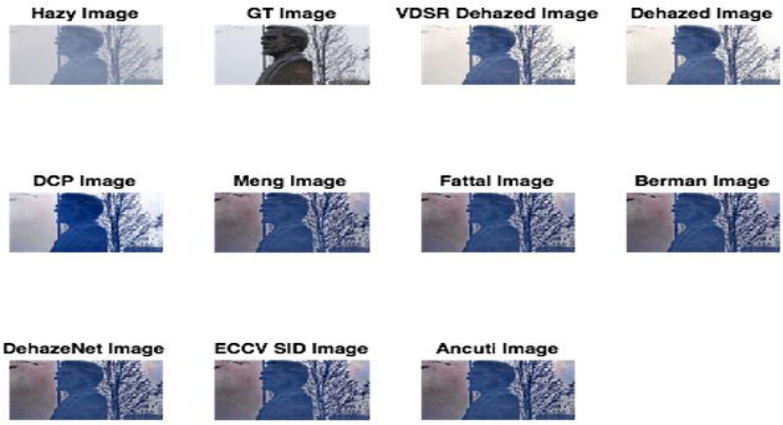

Figure 29. Crop version of figure 27 [17]

4.3 Comparative Analysis

The O-Haze dataset [17] has been used for comprehensive performance evaluation on recent single image dehazing. Few non-homogeneous scenes have been picked randomly from [17]. In figure 30, subjective results are: L-R: the hazy image, He et al. [18], Meng et al. [19], Fattal [20], Cai et al. [29], Ancuti et al. [17], Berman et al. [21] and Ren et al. [22], GT, SIVDSR, and SIVDSRRE. T-B: 11 scene from 45 scene of O-Haze dataset [17]. Table XI presents Quantitative evaluation of figure 30 and computes the SSIM and CIEDE2000 indicating between the ground truth images and the dehazed images produced by the evaluated techniques as mentioned above. Table XII Shows quantitative evaluation of all the 45 set of images of the O-HAZE dataset. This table presents the average values of the SSIM, PSNR and CIEDE2000 indexes, over the entire dataset. Finally, figure 31 elaborates Qualitative Comparative detail insets (cropped version) results as: L-R: the hazy image, He et al. [18], Meng et al. [19], Fattal [20], Cai et al. [29], Ancuti et al. [17], Berman et al. [21] and Ren et al. [22], GT, SIVDSR-Dehaze, and SIVDSR-DehazeRE. T-B: 3 scene scenes (10, 19, 41) from 45 scene of the O-Haze dataset [17].

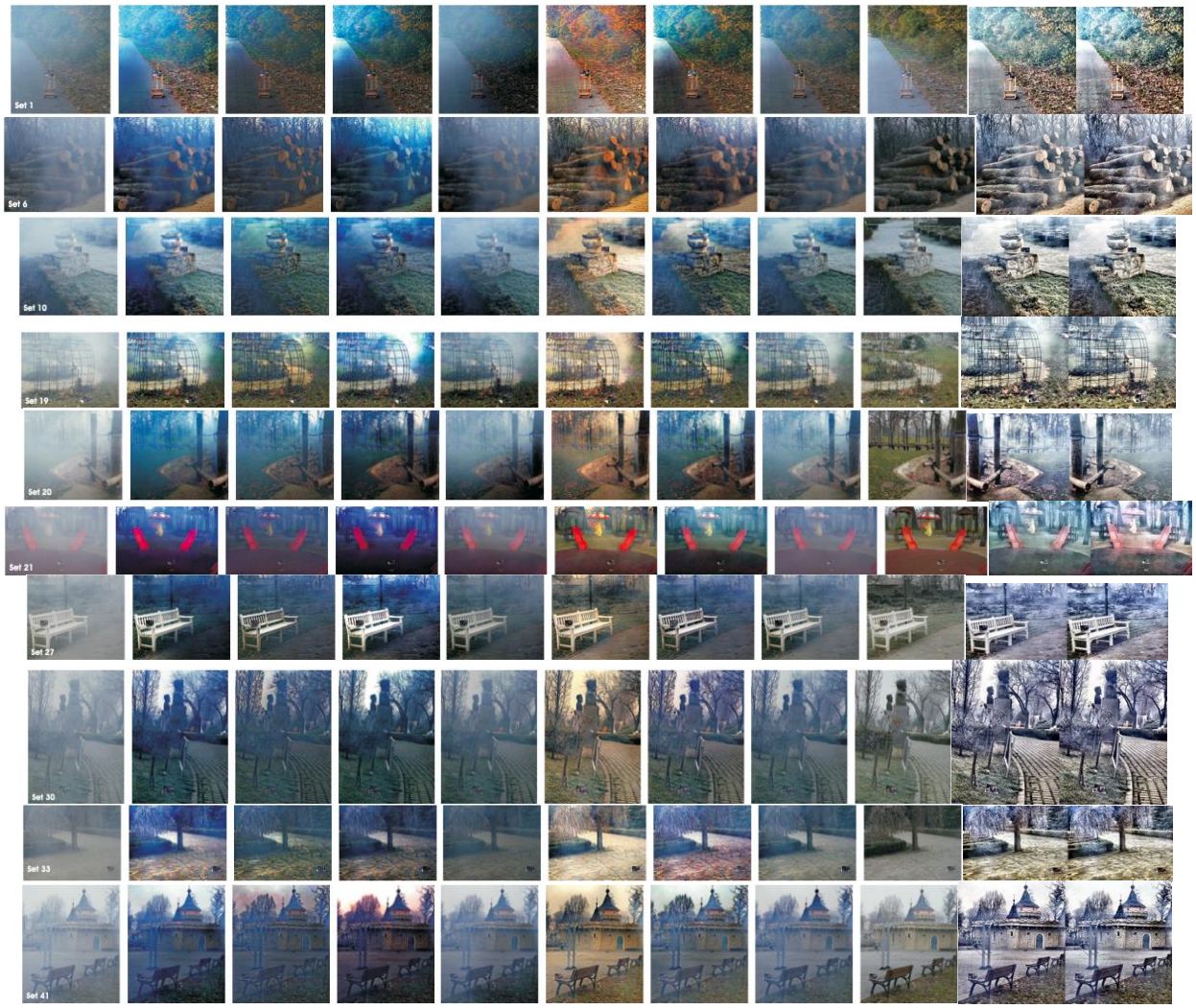

Figure 30. Qualitative ***Comparative results: L-R:*** *the hazy image, He et al. [18], Meng et al. [19], Fattal [20], Cai et al. [29], Ancuti et al. [17], Berman et al. [21] and Ren et al. [22], GT, SIVDSR-Dehaze, and SIVDSR-DehazeRE. T-B: 11 scene from 45 sceneof O-Haze dataset [17].*

Table XI. ***Quantitative evaluation.*** *We randomly picked up 11 sets from our O-HAZE dataset, and computed the SSIM and CIEDE2000 indices between the ground truth images and the dehazed images produced by the evaluated techniques. The hazy images, ground truth and the results are shown in figure 30.*

	He et al. [18]		**Meng et al.**		**Fattal**		**Cai et al.**		**Ancuti et al..**		**Berman et al.**		**Ren et al.**		**SIVDSR-Dehaze(Ours)**		**SIVDSR-DehazeRE (Ours)**	
	SSIM [13]	**CIEDE 2000 [33,34]**	**SSIM**	**CIEDE 2000**	**SSIM**	**CIEDE 2000**	**SSIM**	**CIEDE 2000**	**SSIM**	**CIEDE 2000**	**SSIM**	**CIEDE 2000**	**SSIM**	**CIEDE 2000**	**SSIM**	**CIEDE 2000**	**SSIM**	**CIEDE 2000**
Set 1	0.82	22.37	0.77	21.06	0.73	24.29	0.58	24.42	0.75	20.09	0.76	20.97	0.81	18.17	0.9783	**13.0719**	**0.9823**	16.963
Set 6	0.74	19	0.78	11.44	0.73	21.89	0.59	16.16	0.68	15.53	0.77	12.68	0.72	13.2	0.9807	**11.254**	**0.9812**	13.2884
Set 10	0.78	**15.22**	0.76	16.63	0.75	17.49	0.71	16.17	0.73	19.21	0.72	17.77	0.8	13.7	0.9897	18.8753	**0.9898**	19.371
Set 19	0.81	16.31	0.84	13.37	0.79	21.48	0.72	16.92	0.78	15.55	0.82	14.49	0.83	**12.98**	0.9828	16.6627	**0.9834**	19.7795
Set 2	0.61	23.81	0.72	20.91	0.62	20.73	0.5	23.71	0.78	**12.67**	0.72	19.4	0.63	20.98	0.9886	13.8829	**0.9857**	15.7584

0																		
Set 21	0.69	27.5	0.78	21.13	0.63	28.25	0.71	19.49	0.78	**10.72**	0.72	20.54	0.73	20.26	0.9812	10.7899	**0.9869**	12.1366
Set 27	0.61	21.38	0.68	18.76	0.67	22.37	0.64	17.16	0.77	10.94	0.7	18.41	0.71	14.16	0.9861	**9.498**	**0.9849**	11.9723
Set 30	0.75	18.85	0.74	18.59	0.72	18.46	0.77	12.7	0.83	**11.25**	0.81	14.55	0.82	12.66	0.9829	12.8731	**0.9831**	13.3614
Set 33	0.76	18.54	0.74	15.84	0.76	17.86	0.81	**14.61**	0.61	20.86	0.66	19.39	0.88	10.87	0.9851	15.1021	**0.9851**	15.5605
Set 41	0.77	19.54	0.72	21.45	0.66	23.71	0.84	12.78	0.84	13.02	0.82	14.36	0.88	12.34	0.9853	**11.1101**	**0.985**	11.6285
Set 42	0.79	19.7	0.82	11.03	0.73	13.21	0.58	15.58	0.74	15.37	0.82	**11**	0.72	12.87	0.9841	12.126	**0.9842**	13.1674

Table XII. Quantitative evaluation of all the 45 set of images of the O-HAZE dataset. This table presents the average values of the SSIM, PSNR and CIEDE2000 indexes, over the entire dataset.

	He et al.	Meng et al.	Fattal	Cai et al.	Ancuti et al.	Berman et al.	Ren et al.	SRVDSR-Dehaze	SRVDSR-DehazeRE
SSIM	0.735(7)	0.753(4)	0.707(8)	0.666(9)	0.7470(6)	0.750(5)	0.765(3)	0.9840(2)	**0.9846(1)**
PSNR	16.586(5)	17.443(2)	15.639(7)	16.207(6)	16.855(3)	16.610(4)	**19.068(1)**	15.23(8)	14.13(9)
CIEDE2000	20.745(9)	16.968(5)	19.854(8)	17.348(7)	16.431(4)	17.088(6)	14.670(2)	**13.204(1)**	14.817(3)
Total Ranking	21	11	23	22	13	15	6	**11**	13
Ranking	5	2	7	6	3	4	1	**2**	3

Figure 31. Qualitative ***Comparative detail insets (cropped version) results: L-R:*** *the hazy image, He et al. [18], Meng et al. [19], Fattal [20], Cai et al. [29], Ancuti et al. [17], Berman et al. [21] and Ren et al. [22], GT, SIVDSR-Dehaze, and SIVDSR-DehazeRE. T-B: 3 scene scenes (10, 19, 41) from 45 scene of the O-Haze dataset [17].*

4.4 Computational Complexity Applications:

The proposed algorithm is divided into two parts: i) Atmospheric scattering model [2, 3, 10, 11], ii) VDSR NETWORK [4-5] as in figure 2. The low complexity atmospheric scattering model has computational complexity $O(n^2)$ [6-9, 30]. The VDSR model is faster than other SRCNN methods [4-5]. Thus, it can be concluded that the proposed model works faster in the VDSR framework in comparison with other SRCNN frameworks.

Applications:

a) Image visibility improvement and Edge-preserving smoothing: Here edge-preserving smoothing filters can preserve the key features of an image like an edge and denoise the image. Flash/No-Flash Denoising: It can denoise a no-flash image under the guidance of its flash version.

b) Matting/Guided Feathering: Extracting foreground objects from an image means separating the foreground from the background. It is used in video editing and image processing.

c) Haze Removal: Hazy images are formed due to light scattering with particles in the atmosphere. Haze removal filters will improve the image.

d) Joint Upsampling: Under the guidance of another image, upsampling is done. One application of joint upsampling is the colourization of images.

e) Underwater visibility improvement

4.5 Evaluation and Discussion

A novel image dehazing technique has been presented with a comparative evaluation with the seven state-of-the-art contemporary techniques. In Section 4.3 scenes from the O-HAZE dataset [17] are used in the experiments picked randomly. In figure 4, eleven columns are there; the first column shows hazy images from [17], the second to eight columns are [18,-22, 29, 33], column nine shows ground truth, and columns ten and eleven are the proposed super resolution based dehazing results and followed by enhanced super resolution based dehazing. Furthermore, in figure 31, the comparative cropped detail of scenes 10, 19 and 41, respectively have been examined. In subjective observation, the work of He et al. [18] attains 73.5% of structure information SSIM [13] with low airlight estimation leading to colour shifting. Additionally, low contrast and gloomy images are found. Halo artifacts and gradient reversal effects are prominent. Thus, DCP fails in the O-Haze dataset. In [19], Meng et al. proposed a method based on DCP producing results better than [18] in low noise (PSNR), a low colour difference (CIEDE2000) [33, 34] with good transmission estimation. Undesirable shifting of colour is also prominent in Fattal [20], and in Berman et al. [21], the effect is lessened with sharp edges with the local estimation of airlight and transmission. In Ancuti et al. [17], the resulting images are of good contrast due to efficient multi-scale fusion and local airlight estimation. Ren et al. [22] (column 8 of figure3) and Cai et al. [29] (column 5 of figure 3) depend on learning based techniques. Whereas, in [22] good results are obtained compared to [29]. Finally, the proposed approaches (SR Dehaze, tenth column; and Enhanced SR Dehaze, eleventh column) present clear visible output in both foreground and background. Thus, subjective analysis has been carried out with the seven state-of-the-art techniques [17-22, 29]. They belong to prior based techniques [18-20, 22, 17], and learning based techniques [21, 29]. Most of them, on average, produce meaningful results with halo artifacts, gradient reversals, and colour shifting. Unpleasant, synthetic appearances are inevitable. It should be noted that, with the O-Haze dataset [17] ground truths (GT) are also available, this gives the comparative study a robust validation. But proposed techniques present far better output in comparison to all others. The effectiveness of the proposed techniques is measured with the O-Haze dataset as the objective evaluation with other dehazing techniques. In Table XI, a comparative analysis with the different dehazing techniques prior based [18-21, 29, 27] and learned based techniques [21, 22] with respect to GT and the proposed techniques have been discussed against parameter SSIM, CIEDE2000 [13, 33, 34] as in figure 30. Local patterns of pixel intensities of two images of the same scene are compared in the structural similarity index (SSIM) normalizing luminance and contrast in the range [0-1]; 1 for an absolute similar image, zero indicates no match at all. maximum value 1 for two identical images. CIEDE2000 is a parameter for colour distortion measurement in the range [0-100]; a smaller value for better preservation of colour, and a higher value for high colour distortion.

The O-Haze dataset has 45 scenes, and an average of SSIM, PSNR, CIEDE2000 of the entire dataset scenes has been entered in table XII experimenting with those seven techniques [17-22, 29] and two proposed techniques. Table XII shows our methods outperform other methods in SSIM, and in CIEDE2000. In the case of PSNR, Ren et al [22] give the best performance. The bottom row of Table IX shows that Meng et al [19] outperform other methods (a total of eleven methods) in parametric evaluation (SSIM, PSNR, CIEDE2000). The second and third positions are obtained by the proposed methods. Meng et al [19] obtained 2nd posi-

tion jointly and Ancuti et al [17] secured 3rd position jointly. The following positions are [18, 20, 21, 29]. In nutshell, none of the methods executes better than the others with all 45 images in the O-Haze dataset. The highest value of SSIM and the lowest value for CIEDE2000 are recorded with the proposed methods. To summarise, the above analysis shows the complexity of the single-image based dehazing problem. Moreover, this also has been established that the proposed methods produce convincing results qualitatively and quantitatively. Finally, cropped version scenes of 10, 19, 41 show comparable results, even better.

5. Conclusion

In this article, a single image super resolution based image visibility improvement method has been proposed, which is designed for improving the visibility of digital images captured in turbid atmospheres. Researchers are working to reduce poor visibility and SIVIAs are most prominent but also have challenges of low computational complexity, accurate depth map, and preserving the image quality and structure. The image formation scattering linear model [10] is inverted with a significant change incorporating in-depth map estimation leading to better transmission followed by a clear image. This new method has been compared qualitatively and quantitatively against eight state-of-the-art techniques; VDSR is employed to preserve important structures of the image in depth map estimation. VDSR is a very deep network based on super-resolution. In VDSR, residual learning with extremely high learning rates is adapted to reduce the slow convergence rate with maximizing convergence speed, gradient clipping is used to nail down training stability. VDSR is applicable in image super-resolution, reconstruction, denoising, and compression artifact removal. Due to these properties of VDSR, the depth map is denoised effectively for reducing poor visibility. Enhanced SR Dehazing is a by-product of the above mentioned algorithm. Thus, as a whole two algorithms have been proposed. PSNR, SSIM, BRISQUE, NIQE, and CIEDE2000 are some important parameters to evaluate image quality in VIAs. It is clear from the acquired results that the proposed algorithms are superior in reducing the effect of poor visibility. **Future Direction** -In the future, as shown in table XII there is scope to improve parameter PSNR values so that the ranking of the proposed algorithms will be increased.

Table XIII. Author's Statement

Authors' contributions	Single image super Resolution dehazing image output is obtained with the VDSR network. Both the authors have contributed equally to this work.
Ethical Conflict	There is no conflict of interest in this work.
Funding	No funding has been received for the project.
Data Availability Statement	NA

Table XIV. Abbreviation used

VIA	SIVDSR	SIVDSR-Dehaze	SIVDSR-DehazeRE	TM	CNN	GT
Visibility Improvement Algorithms	Single Image Visibility Super Resolution	Single Image Visibility Super Resolution Dehaze	SIVDSR-Dehaze Residual Enhancement	Transmission Map	Convolution Neural Network	Ground Truth

Table XV. Dataset Used Details

Dataset	O-Haze[17]	Single Image Haze Removal Using Dark Channel Prior. [18]
Statement	It is a collection of 40 outdoor hazy-ground truth images	Canon.jpg has been taken from [18].

References

[1] P. S. Chavez (Jr.), An improved dark-object subtraction technique for atmospheric scattering correction of multispectral data, Remote Sensing and Environment, Elsevier, vol-24(3), pp-459-479,1988

[2]. P. Oakley and B. L. Satherley, “Improving image quality in poor visibility conditions using a physical model for contrast degradation,” IEEE Trans. Image Process., vol. 7, no. 2, pp. 167-179, Feb. 1998.

[3] Simonyan, K., and A. Zisserman. Very Deep Convolutional Networks for Large-Scale Image Recognition. Computational and Biological Learning Society, 2015, pp. 1–14.

[4] J. Kim, J. K. Lee and K. M. Lee, "Accurate Image Super-Resolution Using Very Deep Convolutional Networks," 2016 IEEE Conference on Computer Vision and Pattern Recognition (CVPR), 2016, pp. 1646-1654, doi: 10.1109/CVPR.2016.182.

[5] W. Yang, X. Zhang, Y. Tian, W. Wang, J. Xue and Q. Liao, "Deep Learning for Single Image Super-Resolution: A Brief Review," in IEEE Transactions on Multimedia, vol. 21, no. 12, pp. 3106-3121, Dec. 2019, doi: 10.1109/TMM.2019.2919431.

[6] D. Das, S. S. Chaudhuri and S. Roy, "Dehazing technique based on dark channel prior model with sky masking and its quantitative analysis," 2016 2nd International Conference on Control, Instrumentation, Energy & Communication (CIEC), 2016, pp. 207-210, doi: 10.1109/CIEC.2016.7513741.

[7] Sangita Roy and Sheli Sinha Chaudhuri, “Fast Single Image Haze Removal Scheme Using Self-Adjusting: Haziness Factor Evaluation”, International Journal of Virtual and Augmented Reality (IJVAR), 3 (1), 2019, pp. 42-57.

[8] Sangita Roy and Sheli Sinha Chaudhuri, “WLMS-based Transmission Refined Self-Adjusted No Reference Weather Independent Image Visibility Improvement”, IETE Journal of Research, September 2020. https://doi.org/10.1080/03772063.2019.1662335

[9] S Roy, S S Chaudhuri, Low Complexity Single Color Image Dehazing Technique, Intelligent Multidimensional Data and Image Processing, IGI Global,2018(special session).

[10] H. Koschmieder, Theorie der horizontalen sichtweite, Beitr.Phys. Freien Atm., vol. 12, 1924, pp. 171–181.

[11] E J McCartney, Optics of the Atmosphere: Scattering by Molecules and Particles, New York, NY, USA:Wiley, 1976.

[12] He, Kaiming, et al. "Delving deep into rectifiers: Surpassing human-level performance on imagenet classification." *Proceedings of the IEEE international conference on computer vision*. 2015.

[13] Zhou Wang, A. C. Bovik, H. R. Sheikh and E. P. Simoncelli, "Image quality assessment: from error visibility to structural similarity," in IEEE Transactions on Image Processing, vol. 13, no. 4, pp. 600-612, April 2004, doi: 10.1109/TIP.2003.819861.

[14] Sara, U., Akter, M. and Uddin, M. (2019) Image Quality Assessment through FSIM, SSIM, MSE and PSNR—A Comparative Study. Journal of Computer and Communications, 7, 8-18. doi: 10.4236/jcc.2019.73002.

[15] A. Mittal, A. K. Moorthy and A. C. Bovik, "No-Reference Image Quality Assessment in the Spatial Domain," in IEEE Transactions on Image Processing, vol. 21, no. 12, pp. 4695-4708, Dec. 2012, doi: 10.1109/TIP.2012.2214050.

[16] Mittal, A., R. Soundararajan, and A. C. Bovik. "Making a Completely Blind Image Quality Analyzer." IEEE Signal Processing Letters. Vol. 22, Number 3, March 2013, pp. 209–212.

[17] C. O. Ancuti, C. Ancuti, R. Timofte and C. De Vleeschouwer, "O-HAZE: A Dehazing Benchmark with Real Hazy and Haze-Free Outdoor Images," 2018 IEEE/CVF Conference on Computer Vision and Pattern Recognition Workshops (CVPRW), 2018, pp. 867-8678, doi: 10.1109/CVPRW.2018.00119.

[18] K. He, J. Sun and X. Tang, "Single Image Haze Removal Using Dark Channel Prior," in IEEE Transactions on Pattern Analysis and Machine Intelligence, vol. 33, no. 12, pp. 2341-2353, Dec. 2011, doi: 10.1109/TPAMI.2010.168.

[19] G. Meng, Y. Wang, J. Duan, S. Xiang, and C. Pan. Efficient image dehazing with boundary constraint and contextual regularization. In IEEE Int. Conf. on Computer Vision, 2013.

[20] R. Fattal. Dehazing using color-lines. ACM Trans. on Graph., 2014.

[21] D. Berman, T. Treibitz, and S. Avidan. Non-local image dehazing. IEEE Intl. Conf. Comp. Vision, and Pattern Recog, 2016.

[22] Ren W., Liu S., Zhang H., Pan J., Cao X., Yang MH. (2016) Single Image Dehazing via Multi-scale Convolutional Neural Networks. In: Leibe B., Matas J., Sebe N., Welling M. (eds) Computer Vision – ECCV 2016. ECCV 2016. Lecture Notes in Computer Science, vol 9906. Springer, Cham. https://doi.org/10.1007/978-3-319-46475-6_10

[23] W. Yang, X. Zhang, Y. Tian, W. Wang, J. Xue and Q. Liao, "Deep Learning for Single Image Super-Resolution: A Brief Review," in IEEE Transactions on Multimedia, vol. 21, no. 12, pp. 3106-3121, Dec. 2019, doi: 10.1109/TMM.2019.2919431.

[24] C. Dong, C. C. Loy, K. He, and X. Tang, “Learning a deep convolutional network for image super-resolution,” in Proc. Eur. Conf. Comput. Vis., 2014, pp. 184–199.

[25] C. Dong, C. C. Loy, K. He, and X. Tang, “Image super-resolution using deep convolutional networks,” IEEE Trans. Pattern Anal. Mach. Intell., vol. 38, no. 2, pp. 295–307, Feb. 2016.

[26] A. S. Parihar, Y. K. Gupta, Y. Singodia, V. Singh and K. Singh, "A Comparative Study of Image Dehazing Algorithms," 2020 5th International Conference on Communication and Electronics Systems (ICCES), 2020, pp. 766-771, doi: 10.1109/ICCES48766.2020.9138037.

[27] W. Yang et al., "Advancing Image Understanding in Poor Visibility Environments: A Collective Benchmark Study," in IEEE Transactions on Image Processing, vol. 29, pp. 5737-5752, 2020, doi: 10.1109/TIP.2020.2981922.

[28] C. Chengtao, Z. Qiuyu and L. Yanhua, "A survey of image dehazing approaches," The 27th Chinese Control and Decision Conference (2015 CCDC), 2015, pp. 3964-3969, doi: 10.1109/CCDC.2015.7162616.

[29] B. Cai, X. Xu, K. Jia, C. Qing and D. Tao, "DehazeNet: An End-to-End System for Single Image Haze Removal," in IEEE Transactions on Image Processing, vol. 25, no. 11, pp. 5187-5198, Nov. 2016, doi: 10.1109/TIP.2016.2598681.

[30] Ph.D. Thesis, Sangita Roy, Development of Improved Visibility Restoration Techniques using Various Intensity Parameter Tuning, ETCE Department, Jadavpur University, July 2021.

[31] J. -B. Huang, A. Singh and N. Ahuja, "Single image super-resolution from transformed self-exemplars," 2015 IEEE Conference on Computer Vision and Pattern Recognition (CVPR), 2015, pp. 5197-5206, doi: 10.1109/CVPR.2015.7299156.

[32] J. Yang, J. Wright, T. S. Huang and Y. Ma, "Image Super-Resolution Via Sparse Representation," in IEEE Transactions on Image Processing, vol. 19, no. 11, pp. 2861-2873, Nov. 2010, doi: 10.1109/TIP.2010.2050625..

[33] G. Sharma, W. Wu, and E. Dalal. The ciede2000 color-difference formula: Implementation notes, sup- plementary test data, and mathematical observations. *Color Research and Applications*, 2005, https://doi.org/10.1002/col.20070.

[34] S Westland, C Ripamonte, Computational Colour Science using MATLAB, Wiley-IS&T Series in Imaging Science and Technology.

[35] Y. Y. Schechner, S. G. Narasimhan and S. K. Nayar, "Instant dehazing of images using polarization," Proceedings of the 2001 IEEE Computer Society Conference on Computer Vision and Pattern Recognition. CVPR 2001, 2001, pp. I-I, doi: 10.1109/CVPR.2001.990493.

[36] S. G. Narasimhan and S. K. Nayar, "Chromatic framework for vision in bad weather," Proceedings IEEE Conference on Computer Vision and Pattern Recognition. CVPR 2000 (Cat. No.PR00662), 2000, pp. 598-605 vol.1, doi: 10.1109/CVPR.2000.855874.

[37] CIE. Improvement to industrial colour-difference evaluation. Vienna:CIE Publication No. 142-2001, Central Bureau of the CIE; 2001.

[38] R. T. Tan, "Visibility in bad weather from a single image," 2008 IEEE Conference on Computer Vision and Pattern Recognition, 2008, pp. 1-8, doi: 10.1109/CVPR.2008.4587643.

[39] Kopf, Johannes, et al. "Deep photo: Model-based photograph enhancement and viewing." *ACM transactions on graphics (TOG)* 27.5 (2008): 1-10.

[40] S Roy, S S Chaudhuri, Single Image Very Deep Super Resolution (SIVDSR) Dehazing, BECITHCON 2021, 4-5 December 2021.

[41] S Roy, Single Image DnCNN Visibility Improvement (SImDnCNNVI), Scientific Visualization, volume 14, number 3, pages 92 – 106, September 19th 2022, https://doi.org/10.26583/sv.14.3.07.